# A MULTIMODAL LLM APPROACH FOR VISUAL QUESTION ANSWERING ON MULTIPARAMETRIC 3D BRAIN MRI

# **Anonymous authors**

Paper under double-blind review

#### **ABSTRACT**

We introduce mpLLM, a prompt-conditioned hierarchical mixture-of-experts (MoE) architecture for visual question answering over multiparametric 3D brain MRI (mpMRI). mpLLM routes across modality-level and token-level projection experts to fuse multiple interrelated 3D modalities, enabling efficient training without image-report pretraining. To address limited image-text paired supervision, mpLLM integrates a synthetic visual question answering (VQA) protocol that generates medically relevant VQA from segmentation annotations, and we collaborate with medical experts for clinical validation. mpLLM outperforms strong medical VLM baselines by 5.3% on average across multiple mpMRI datasets. Our study features three main contributions: (1) the first clinically validated VQA dataset for 3D brain mpMRI, (2) a novel multimodal LLM that handles multiple interrelated 3D modalities, and (3) strong empirical results that demonstrate the medical utility of our methodology. Ablations highlight the importance of modality-level and token-level experts and prompt-conditioned routing. We have included our source code in the supplementary materials and will release our dataset upon publication.

#### 1 Introduction

Multiparametric MRI (mpMRI) plays a significant role in diagnosing, grading, treating, and assessing treatment responses for brain tumors and other intracranial lesions (Sawlani et al., 2020; Wang et al., 2022a; Cherubini et al., 2016). Describing imaging that involves a complex pattern of brain lesions across multiple regions can be challenging and time-consuming for clinicians. Consequently, several studies have been conducted to develop image recognition and localization models to support clinicians (Ghadimi et al., 2025; Rathore et al., 2018; Wang et al., 2022a; Li et al., 2023c; Osman, 2019).

However, existing models have limited clinical utility because clinicians cannot effectively pose natural language queries about mpMRI. While 3D vision-language models (VLMs) have been developed for other imaging domains, current architectures do not naturally leverage the interdependencies among mpMRI modalities (Li et al., 2023a; Wu et al., 2023; Bai et al., 2024; Xin et al., 2025). Additionally, the standard multi-image approach multiplies the number of vision tokens by the number of images, which significantly increases computational constraints (Wu et al., 2023).

We introduce mpLLM, a prompt-conditioned hierarchical mixture-of-experts (MoE) for VQA over mpMRI. Conditioned on the input question, a router allocates computation across modality-level experts and token-level projection experts to achieve parameter-efficient fusion of multiple interrelated 3D modalities. Unlike modality-specific or modality-agnostic vision encoders, our low-level components are lightweight projection functions that train end-to-end with the language model during fine-tuning. Additionally, the multimodal LLM processes a single fused vision token representation, which dramatically reduces the GPU memory usage.

To address limited image-text paired supervision, we pair mpLLM with a synthetic VQA protocol that derives medically relevant VQA from segmentation annotations, and we obtain clinician validation of both the generated data and model responses. In contrast to prior works, we fine-tune our model using next-token prediction directly on the VQA dataset without pretraining on a paired imaging-report

056

060

061

062

063 064

065

066

067

069

070 071

073

075

076

077

079

081

083

084

085

087

090

091

092

094

095

096

098

100 101

102

103

104

105

107

Figure 1: High-level comparison between LLaVA-Med and mpLLM. While LLaVA-Med uses a standard projection layer, our method uses a hierarchical MoE block which ingests both the prompt and imaging to produce prompt-conditioned vision tokens that leverage all the 3D modalities.

dataset. We also train a multi-task head end-to-end with the multimodal LLM for improved task proficiency and more reliable evaluation. In summary, our research makes these key contributions:

- 1. In collaboration with medical experts, we introduce a synthetic VQA protocol that produces the first clinically validated VQA dataset for 3D brain mpMRI.
- 2. We design mpLLM, a multimodal LLM that uses a prompt-conditioned hierarchical MoE to effectively leverage the interdependence between 3D modalities in mpMRI.
- 3. Strong empirical results that support our methodology as a foundation for future research with multimodal LLMs in brain mpMRI.

#### 2 Related Work

Medical vision-language models Most vision-based medical multimodal LLMs can be broadly classified into CLIP-based discriminative models (Radford et al., 2021; Wang et al., 2022b; Eslami et al., 2023; Zhang et al., 2023a; Xu et al., 2024; Zhou et al., 2024; Huang et al., 2023) and LLM decoder-based generative models (Zhang et al., 2023b; Li et al., 2023a; Moor et al., 2023). Although discriminative models have proven helpful for various image recognition tasks, they possess limited utility in generation tasks such as VQA or report generation. Several popular generative models including MedVInt (Zhang et al., 2023b), LLaVA-Med (Li et al., 2023a), and MedFlamingo (Moor et al., 2023) share very similar architectures. However, these architectures and many others (Liu et al., 2024c; Lin et al., 2023; Li et al., 2023b; Zhu et al., 2024a; Lin et al., 2025; Zhang et al., 2025b; Nath et al., 2024; Guo et al., 2025) are designed specifically for 2D medical imaging and are not tailored to handle multiple 3D medical image modalities.

Although several 3D VLMs exist for natural images (Zhu et al., 2024b; Li et al., 2024b; Zhu et al., 2023), they require access to extremely large annotated datasets, which are often unavailable in medical contexts. While a few 3D VLMs have been developed for medical imaging, these methods have certain limitations. In one recent paper, researchers adapted the LLaVA-Med architecture to utilize spatial pooling and pretrain a 3D vision encoder with 700k radiology images (Bai et al., 2024). In another paper, researchers pretrain segmentation modules to generate brain imaging reports (Lei et al., 2024). In recent work, researchers exploit vision-language pretraining for CT report generation (Liu et al., 2023a; Chen & Hong, 2024; Blankemeier et al., 2024; Xin et al., 2025; Cao et al., 2025). However, these prior works assume a large paired imaging-report pretraining dataset, which is infeasible to collect and imposes a significant training burden.

Furthermore, previous methods focus on report generation instead of VQA, leading to less precise feedback regarding model strengths and weaknesses. Additionally, some models train directly on segmentation annotations (Lei et al., 2024; Rui et al., 2024), which are impractical to obtain, especially for novel use cases. Moreover, none of the previously discussed methods are tailored to handle multiple interdependent 3D image modalities, like in mpMRI, as input.

**Mixture-of-experts** Previous work in MoE has concentrated on training and inference efficiency (Shazeer et al., 2017; Lepikhin et al., 2020; Fedus et al., 2022; Zoph et al., 2022; Liu et al., 2024a),

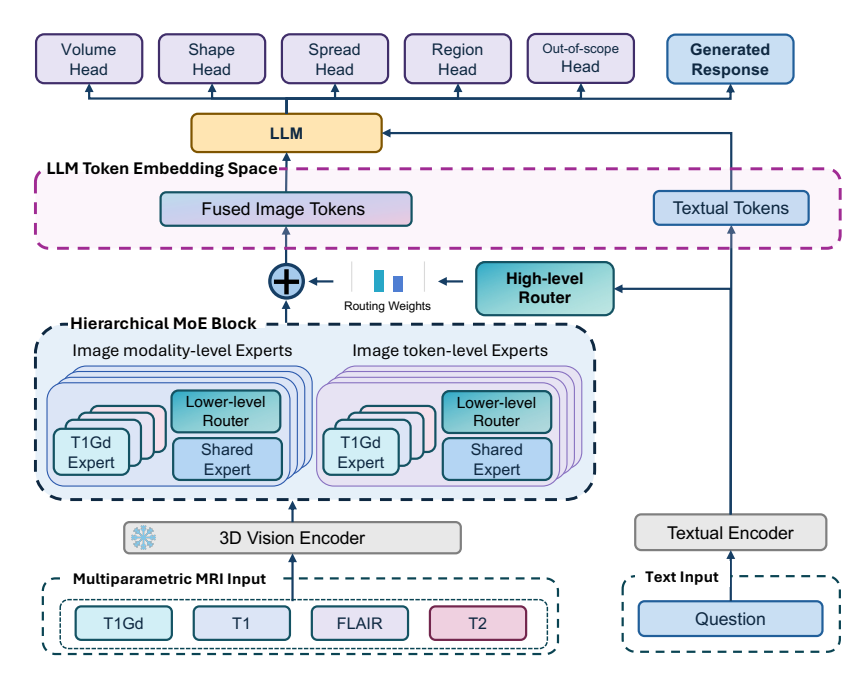


Figure 2: Detailed overview of our mpLLM pipeline.

transfer learning (Li et al., 2022; Zhong et al., 2022), class imbalance (Han et al., 2024), and multidomain information (Zhang et al., 2024). There have also been earlier efforts with multimodal LLMs, covering sparsity learning (Lin et al., 2024), task interference (Shen et al., 2025), and embedding models (Li & Zhou, 2024). Related to our work, several studies have employed MoE with VLMs to select between vision encoders and vision-language projections (Li et al., 2025; Zong et al., 2024; Wang et al., 2023; Ma et al., 2025). However, these studies address two modalities and do not account for interactions between different 3D image modalities, which present additional challenges our work seeks to address.

MoE also has various applications in the medical field. These applications include addressing missing modalities (Yun et al., 2025; Novosad et al., 2024; Liu et al., 2024d), fairness (Wang et al., 2025), pediatric care (Huy et al., 2025), parameter reduction and efficiency (Jiang et al., 2024; Nathani et al., 2024), and super resolution (Lin et al., 2021). Additionally, several studies have focused on the segmentation of multimodal medical imaging (Zhang et al., 2025a; Jiang & Shen, 2024). However, no existing research has explored using MoEs for multiple interrelated 3D image modalities. This area is particularly complex due to the need to project multiple interrelated vision modalities into the language modality.

Medical VQA Datasets One of the primary challenges in report generation is evaluation: lexical metrics such as BLEU, ROUGE-L, and BERTScore have been shown to correlate poorly with radiologist evaluations (Yu et al., 2023). In contrast, VQA allows for more granular and interpretable model evaluation. While there are several medical VQA datasets, many focus on 2D imaging (Liu et al., 2024b; 2021; He et al., 2020; Lau et al., 2018). In a prior work, researchers used a scene graph generator to generate surgical VQA (Yuan et al., 2024). In a recent work, researchers extracted multi-task questions from structured lung cancer screening data (Niu et al., 2025). However, there is no existing VQA dataset for 3D brain mpMRI due to a significant lack of source data for VQA extraction. In our work, we remedy this by leveraging publicly available segmentation annotations as source data.

#### 3 METHODOLOGY

Brain mpMRI has several 3D imaging modalities. Given a specific 3D image modality  $I_m \in R^{C \times D \times H \times W}$ , where m, C, D, H, and W represent the modality, channel, depth, height, and width respectively, we derive the image modality embedding  $v_m = h(I) \in R^{N_I \times d_I}$ . Here, h denotes the vision encoder,  $N_I$  indicates the number of image tokens produced by the vision encoder, and  $d_I$ 

represents the vision encoder token embedding dimension. We pass the image modality embeddings through a spatial pooling layer, which reduces the number of tokens, and concatenate them for all the image modalities before passing them to the hierarchical MoE.

Given the concatenated image modality embeddings  $v \in R^{N_I \times N_m \times d_I}$  where  $N_m$  represents the number of image modalities, we derive the projected image modality embedding  $e = MoE(v,t) \in R^{N_I \times d_T}$  where MoE denotes the hierarchical MoE, t represents the text prompt, and  $t_T$  represents the LLM embedding layer dimension.  $t_T$  is then provided as a soft prompt to the LLM for multi-task prediction and text generation. A detailed visualization of our approach can be seen in Figure 2.

#### 3.1 HIERARCHICAL MIXTURE-OF-EXPERTS FOR MULTIPARAMETRIC MRI PROJECTION

**High-level router** Our hierarchical MoE architecture includes a high-level router h that assigns weights over a set of high-level experts  $\{\mathcal{E}_1^{(h)},...,\mathcal{E}_N^{(h)}\}$ , where N is the number of high-level experts. These experts operate at the image modality and image token levels. The router is implemented as a two-layer MLP that takes as input the final hidden state of the language model corresponding to the text prompt t. It produces a normalized weight distribution over experts:  $\pi^{(h)}(t) = softmax(h(t)) \in \mathbb{R}^N$ . Since task information is embedded within the text prompt, the router implicitly infers the task, enabling the high-level experts to specialize in different task proficiencies.

**High-level image modality-level and image token-level experts** Our hierarchical MoE includes high-level experts operating at different granularity levels: image modality-level and image token-level. Each high-level expert consists of a two-layer MLP low-level router l and a set of associated low-level experts  $\{W_1^{(l)},...,W_M^{(l)}\}$  where M is the number of low-level experts.

The image modality-level expert takes as input the concatenated [CLS] tokens from all image modalities (e.g., T1, T2), and outputs image modality-level weights over the corresponding low-level experts:  $\pi^{(l)}(v) = sigmoid(l(v)) \in R^M$ . In contrast, the token-level expert receives the i-th position image tokens from all image modalities as input and outputs image token-level weights over the low-level experts for position i:  $\pi^{(l)}(v) = sigmoid(l(v)) \in R^{M \times N_I}$ . As discussed in prior work (Li et al., 2024a), providing weights at different granularities improves task performance by enhancing domain generalizability.

Low-level image modality-specific and image modality-agnostic (shared) experts Each low-level expert W represents a projection transformation from the vision encoder embedding space to the LLM embedding space:  $W:R^{N_I\times d_I}\to R^{N_I\times d_T}$ . We utilized a simple linear transformation for the projection transformation as in the original LLaVa paper (Liu et al., 2023b). Each image modality embedding is processed through a modality-specific expert and a modality-agnostic (shared) expert. The modality-specific expert emphasizes extracting image modality-specific features, whereas the modality-agnostic expert focuses on deriving common features from all image modalities. The parameters for the modality-specific expert are unique to each image modality (T1Gd, T1, T2, and FLAIR), while those for the modality-agnostic expert are consistent across all image modalities.

Each image modality is passed through both low-level experts and then summed embedding dimension-wise. To balance contributions from each image modality and prevent mode collapse towards a single image modality, the low-level router generates weights that total 1 for both experts. The overall formulation for the hierarchical MoE is as follows:

$$MoE(v,t) = \sum_{n \in [N]} \pi_n^{(h)} \sum_{m \in [N_m]} \pi_m^{(l,n)} W_{m,n}(v_m) + (1 - \pi_m^{(l,n)}) W_{shared,n}(v_m)$$
(1)

where n represents the high-level expert and m represents the image modality. We considered several different hyperparameters with our MoE implementation, including the number of high-level experts, prompt information in high-level and/or low-level routers, the number of layers in the low-level experts, and others. Our validation experiments on the GLI dataset found that the optimal number of high-level experts was 16, corresponding to the number of labels times the number of tasks.

Table 1: Statistics for the synthetic VQA datasets.

2	1	8
2	1	9
2	2	0
2	2	1

Dataset	# questions	# mpMRI	# unique questions	# unique answers
GLI	38,904	1,621	38,023	36,773
MET	11,718	651	11,607	11,284
GoAT	24,318	1,351	23,859	23,223

The fused image token embeddings are combined with the text prompt token embeddings. Then, these embeddings are input into the LLM decoder at the token embedding layer for multi-task prediction and text generation.

#### 3.2 Training objectives

# 2.2.1

# 3.2.1 SYNTHETIC VQA PROTOCOL

Because of the lack of brain mpMRI VQA data, we propose a novel method of synthetic VQA generation that leverages the publicly available brain mpMRI segmentation data. To generate relevant VQA data, we consult with clinicians to identify important topics that can be extracted from the label masks, focusing on mask volume relative to brain volume (Kaifi, 2023), brain region localization (Lau et al., 2018), shape (Ismail et al., 2018), and spread (Islam et al., 2019). For each label mask, we compute the quantities using standard formulas and validate the thresholds with synthetic masks and a subset of data. To emulate the subjectivity found in medical reports, we categorize each of the quantities based on their magnitude using terminology similar to that found in medical reports. Rather than using an LLM, we employ a rules-based method to assign medical terms to the quantities, ensuring our approach is clinically relevant and highly reliable. We assign "N/A" if the label is not found.

**Volume** To calculate the relative mask volume, we determine the number of mask pixels and divide by the number of brain pixels in the volume (which are the nonzero pixels in the skull-stripped T1 image modality). The subjective labels we use are "< 1%", "1 - 5%", "5 - 10%", "10 - 25%", "10 - 25%", "10 - 25%", and "10 - 25%", and "10 - 25%", "10

**Region** We use the conform function from the Nibabel python library (Abraham et al., 2014) to put the BraTS volumes and the LPBA40 atlas (Shattuck et al., 2008) in the RAS space. We then overlay the atlas on each mask volume and, based on their intersection, extract the following brain regions: "frontal", "parietal", "occipital", "temporal", "limbic", "insula", "subcortical", "cerebellum", and "brainstem".

**Shape** We first quantify each mask's overall size and compute classical 3-D shape metrics (sphericity, elongation, flatness, solidity, compactness). If the mask is tiny, it is classified as "focus"; otherwise, we classify it as "round," "oval," "elongated," or "irregular" by comparing its sphericity and elongation values to empirically chosen thresholds that correspond to near-sphere, mildly flattened, and strongly stretched geometries.

**Spread** We identify all disconnected islands, noting the largest as the "core," and compute what proportion of the total mask volume it occupies. If there is only one island, the pattern is "single lesion"; if multiple islands are present but the core retains  $\geq 70\%$  of the volume, it is described as "core with satellite lesions"; otherwise, when no dominant island exists, the distribution is marked "scattered lesions."

Question-answer pair generation After computing the previous quantities for each label mask, we create a dataset that simulates the natural variability of human input. First, we consider all combinations of the four major tasks to create multi-task question-answer pairs. After we have the 15 question-answer pair types, we use ChatGPT-40 to generate approximately 3000 perturbations of each question-answer pair (without affecting the label and answer term) that emulates the language a clinician would use. We also add question-answer pairs with partially out-of-scope and completely out-of-scope tasks to improve the model's self-awareness of its capabilities. Thus, for each label

and mpMRI in each dataset, we sample four multitask question-answer pairs without replacement such that each major task is addressed in at least one question-answer pair, one partially out-of-scope question-answer pair, and one completely out-of-scope question-answer pair. Examples of generated question-answer pairs can be seen in the Appendix in Table 5. The answers are used as supervision for next-token prediction for the multimodal LLM.

# 3.2.2 Multi-task heads

For increased task proficiency and more accurate task evaluation, we train a multi-task head end-toend with the multimodal LLM. After providing the soft-prompt to the multimodal LLM, we extract the hidden state from the last layer and apply task-specific heads (which consist of a single linear layer) to generate multi-task predictions. For volume, shape, spread, and out-of-scope task identification, the task is multi-class classification, and the associated loss is categorical cross-entropy; whereas for region localization, the task is multi-label classification, and the associated loss is multi-label binary cross-entropy. These losses are added to the next-token prediction loss to produce our multi-task loss:

$$\mathcal{L} = \mathcal{L}_{\text{Next-token}} + \mathcal{L}_{\text{Volume}} + \mathcal{L}_{\text{Region}} + \mathcal{L}_{\text{Shape}} + \mathcal{L}_{\text{Spread}} + \mathcal{L}_{\text{Out-of-scope}}$$
 (2)

#### 4 EXPERIMENTS

#### 4.1 Datasets details

For our synthetic VQA protocol, we leverage the Brain Tumor Segmentation (BraTS) challenge (LaBella et al., 2024), which provides a standardized benchmarking environment for automated brain tumor segmentation. All datasets comprise of co-registered multiparametric MRI scans (T1, T1Gd, T2, FLAIR) at 1mm³ resolution, skull-stripped and manually annotated by experts. To enable fair comparison and manage GPU memory, all BraTS sequences were resampled to  $32 \times 256 \times 256$ . This allowed for compatibility with baseline methods, such as M3D (Bai et al., 2024) and Med3DVLM (Xin et al., 2025). We consider three challenges in BraTS: GLI, MET and GoAT. The challenges are collected from over ten institutions and encompass diverse pathological contexts and imaging protocols.

**GLI (Adult Glioma Post Treatment)** focuses on post-treatment diffuse glioma segmentation and consists of multi-institutional routine post-treatment clinically-acquired multiparametric mpMRI scans of glioma. The task requires the delineation of enhancing tumor (ET), non-enhancing tumor core (NETC), surrounding FLAIR hyperintensity (SNFH), and resection cavity (RC) (de Verdier et al., 2024).

MET (Brain Metastases) contains a retrospective compilation of treatment-naive brain metastases mpMRI scans obtained from various institutions under standard clinical conditions. The challenge addresses the segmentation of small metastatic lesions using a 3-label system (NETC, SNFH, ET) and demonstrates variable tumor component distribution across cases (Moawad et al., 2024).

**GoAT** (Generalizability Across Tumors) assesses algorithmic generalizability across different tumor types (i.e., different number of lesions per scan, lesion sizes, and locations in the brain), institutions (i.e., different MRI scanners, acquisition protocols), and demographics (i.e., different age, sex, etc.). The challenge uses consistent labels (necrosis, edema/invaded tissue, and enhancing tumor) despite varying tumor morphology to evaluate algorithm adaptability to new disease types with limited training data (de Verdier et al., 2024; Moawad et al., 2024; LaBella et al., 2023; Kazerooni et al., 2024; Adewole et al., 2023).

To generate the train, validation, and test sets, we randomly sample 80%, 10%, and 10% from the imaging studies. For GLI we generated 31,104, 4,176, and 3,624 question-answer pairs for the train, validation, and test sets based on 1,621 mpMRIs. For MET, we generated 9,090, 1,368, and 1,260 question-answer pairs for the train, validation, and test sets, based on 651 mpMRIs. For GoAT, we generated 19,440, 2,430, and 2,448 question-answer pairs for the train, validation, and test sets, based on 1351 mpMRIs.

**Clinical validation** We collaborated with a radiologist who annotated 10 multiparametric MRIs (mpMRIs) from the BraTS-GLI test set, with questions spanning four tasks and four labels per case,

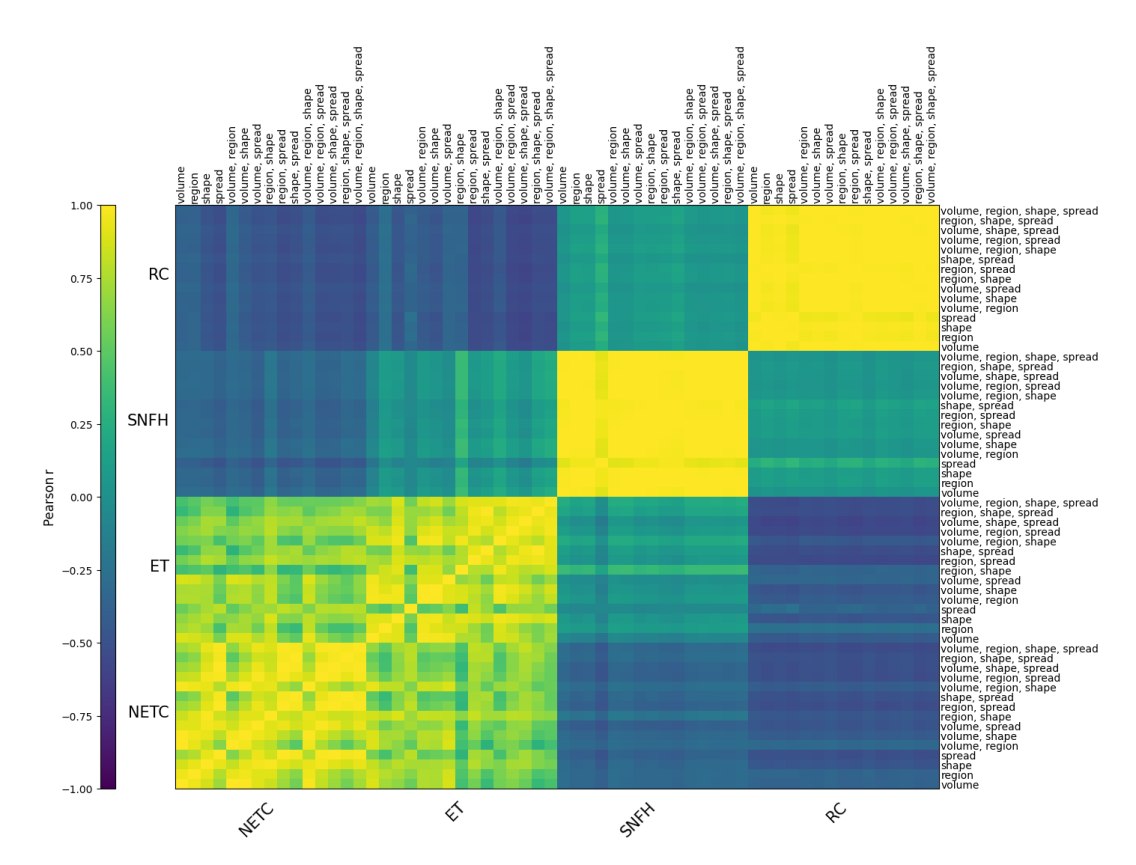


Figure 3: Heatmap for correlation between high-level expert weight vectors for standard prompts in the GLI dataset. NETC = non-enhancing tumor core, ET = enhancing tissue, SNFH = surrounding FLAIR hyperintensity, RC = resection cavity.

yielding a total of 160 questions. We evaluated the inter-annotator agreement between the clinician and our synthetic annotations using the Kappa score, which was 50.4, indicating moderate agreement. To contextualize the value, inter-annotator segmentation agreement for substructures in post-operative glioma typically ranges between 30.0–40.0 Jaccard score (Visser et al., 2019), indicating the difficulty of this task. While no directly comparable study exists for glioma terminology, a relevant meta-analysis of expert inter-annotator agreement on breast cancer terminology reported a median mean Kappa score of 43.8 (Antonio & Crespi, 2010). Furthermore, to assess the quality of our synthetic questions, the same radiologist evaluated the clarity of 160 synthetic questions from the same 10 mpMRIs using a binary scoring system (1 = valid, 0 = invalid). The synthetic questions achieved a 92.2% validity rate, indicating high acceptability.

More statistics about the synthetic datasets can be seen in Table 1, and more details can be found in Appendix A, B, C.

#### 4.2 EXPERIMENTAL SETTINGS

**Models** In our experiments, we utilized the Phi-3-Mini-4K-Instruct LLM. We also explored utilizing the Llama models and chose Phi-3 because of the increased efficiency and negligible performance benefits of the Llama models. For versatility and generality, we utilize the 3D Vision Transformer (3D ViT) (Dosovitskiy et al., 2020) as the vision encoder and use medically pretrained weights (Bai et al., 2024).

**Training** We fine-tune the multimodal LLM using the loss defined in Equation 2 on the VQA training dataset. We freeze the vision encoder while unfreezing the hierarchical MoE and LLM weights. We train the model on the train dataset for 2 epochs. The LLM is trained with LoRA, setting r to 16 and alpha to 32, with a dropout of 0.1. We employ a cosine learning rate scheduler that starts at a learning rate of  $2.0 \times 10^{-4}$ .

Table 2: Comparison of task performance for all models on all datasets with accuracy metric with standard deviation.

Dataset	Method	Volume	Region	Shape	Spread	Mean
	RadFM (Wu et al., 2023)	14.5±0.9	78.1±0.4	15.1±0.9	13.7±0.9	$30.3 \pm 0.4$
CLI	Med3DVLM (Xin et al., 2025)	$43.1 {\pm} 1.2$	$76.7 \pm 0.4$	$47.6 \pm 1.2$	$42.9{\pm}1.3$	$52.6 \pm 0.7$
GLI	M3D (Bai et al., 2024)	$54.3 \pm 1.2$	$81.3 \pm 0.4$	$58.9 \pm 1.2$	$52.9 \pm 1.3$	$61.9 \pm 0.7$
	LLaVA-Med (Li et al., 2023a)	$54.8 \pm 1.2$	$81.2 \pm 0.4$	$58.9 \pm 1.2$	$53.5 {\pm} 1.2$	$62.1 \pm 0.7$
	mpLLM (Ours)	$71.1 \pm 1.1$	$\textbf{84.7} \!\pm\! \textbf{0.3}$	$65.1{\pm}1.1$	$62.7 \pm 1.2$	$\textbf{70.9} \!\pm\! \textbf{0.6}$
	RadFM	19.2±1.5	69.6±1.0	16.7±1.6	10.8±1.3	29.1±0.8
MET	Med3DVLM	$55.2 \pm 2.0$	$69.4 \pm 1.0$	$41.9 \pm 2.0$	$35.9 {\pm} 1.9$	$50.6 \pm 1.0$
NIEI	M3D	$67.5 \pm 1.9$	$73.6 \pm 0.9$	$57.5 \pm 1.9$	$41.2 \pm 2.0$	$60.0 \pm 1.0$
	LLaVA-Med	$70.1 \pm 1.8$	$73.3 \pm 1.0$	$58.8 {\pm} 1.9$	$41.7 \pm 2.1$	$61.0 \pm 1.0$
	mpLLM (Ours)	$\textbf{74.1} {\pm} \textbf{1.8}$	$75.8{\pm}0.9$	$59.1 \pm 1.9$	$49.0 \pm 2.1$	$64.5 {\pm} 1.0$
	RadFM	18.2±1.1	$64.4 \pm 0.5$	37.3±1.5	29.6±1.3	$37.4 \pm 0.7$
GoAT	Med3DVLM	$40.9 \pm 1.4$	$65.6 \pm 0.5$	$66.3 \pm 1.4$	$58.1 \pm 1.4$	$57.7 \pm 0.7$
GOAI	M3D	$63.9 \pm 1.3$	$73.7 {\pm} 0.6$	$\textbf{84.1} \!\pm\! \textbf{1.1}$	$72.7 {\pm} 1.3$	$73.6 \pm 0.6$
	LLaVA-Med	$55.2 \pm 1.5$	$71.6 \pm 0.6$	$83.8 {\pm} 1.1$	$72.8 {\pm} 1.3$	$70.9 \pm 0.7$
	mpLLM (Ours)	$69.8 \pm 1.3$	$\textbf{77.4} \!\pm\! \textbf{0.5}$	$82.4 \pm 1.1$	$74.9 \pm 1.3$	$76.1 \pm 0.6$

Table 3: Ablation study on the MoE architecture on the GLI validation set with accuracy metric.

Modality-level	Token-level	Prompt-based	Task
MoE	MoE	MoE weights	Mean
X	Х	Х	68.7
$\checkmark$	×	×	69.1
X	$\checkmark$	×	69.9
$\checkmark$	$\checkmark$	$\checkmark$	70.4

Baseline models We compare our approach to several baseline models, including LLaVA-Med (Li et al., 2023a), M3D (Bai et al., 2024), Med3DVLM (Xin et al., 2025), and RadFM (Wu et al., 2023)<sup>1</sup>. To process the multiple 3D MRI image modalities, we use a multi-image approach, in which we concatenate the image tokens generated from each MRI image modality from a shared projection layer and vision encoder (Wu et al., 2023). Because LLaVA-Med is not implemented with a 3D vision encoder, to ensure a fair comparison, we test it with our model's vision encoder (Bai et al., 2024). Similar to our method, the vision encoder is frozen and only the projection layer and LLM are trainable. To provide a comparison to our model's multi-task heads, which are trained end-to-end with the rest of our framework, we independently train a new multi-task head. We use a Phi3 language model with multi-task heads to predict the multi-task outputs given the prompt and text generation. The model is trained on our train dataset and had 99.8% accuracy on the validation set. Other hyperparameter settings mirror our method as closely as possible to ensure a fair comparison.

**Evaluation** For evaluating the models' task proficiency, we use accuracy for volume, shape, spread, and out-of-scope tasks, and per-label accuracy for the region task. We estimate the standard deviation using 500 bootstrap resamples.

**Computing environment** All our experiments were mainly conducted using a single NVIDIA A100 GPU on an internal cluster. Training our model on the GLI dataset took roughly 8 hours.

Table 4: Model comparison with multi-task loss on the GLI validation set with accuracy metric.

Method	Task Mean
mpLLM without multi-task loss	67.4
mpLLM with multi-task loss	70.4

## 4.3 RESULTS

All model results across the evaluated datasets are presented in Table 2. Our model consistently achieves strong performance across all task categories and datasets, outperforming the second-best model by an average margin of 5.3%. Furthermore, it ranks first in nearly all sub-categories and datasets, highlighting both its broad capabilities and strong generalizability. We also validated model performance on the clinically annotated subset and graded the top two models' responses for sufficiency, which can be seen in Table 10 and Table 11 respectively in the Appendix, and note that our model outperforms the baselines. Examining the memory usage, our model only required approximately 20 GB of GPU memory during training and inference – significantly less than M3D, LLaVA-Med, and Med3DVLM, all of which exceed 40 GB – suggesting the computational benefits of a fused vision token representation. In our experiments, we also noticed that the top three models had above a 99.8% accuracy on out-of-scope task identification, which suggests our dataset was effective at hallucination mitigation.

# 4.4 Ablation studies

The ablation study on the MoE architecture is in Table 3. Image modality-level and token-level high-level MoE experts perform better than the single projection layer baseline approach. A weighted combination of the different high-level experts conditioned on the text prompt performs the best, which is what our hierarchical MoE architecture utilizes.

To qualitatively evaluate our architecture, we construct all 60 template task prompts from our GLI dataset (four labels  $\times$  15 task combinations = 60 template prompts) and input them into our model's high-level router to generate high-level expert weight vectors. We then calculate the correlation between these weight vectors and generate a heatmap, which is in Figure 3. There's high correlation between expert weight vectors within the same label, suggesting similar image features are extracted. For labels that are closer anatomically, such as non-enhancing tumor core and enhancing tissue, there is also relatively high correlation between the expert weight vectors. This is reasonable because of their close proximity anatomically, which suggests similar extracted image features. For labels like resection cavity and surrounding FLAIR hyperintensity that are more diverse anatomically from the other labels, there's much lower correlation, which again is sensible.

In Table 4, we see a comparison of our model performance trained with our multi-task loss versus the next-token prediction baseline loss. Clearly, there is a significant performance improvement with our multi-task loss.

## 5 Conclusion

We present mpLLM, a multimodal LLM with prompt-conditioned hierarchical MoE that routes across modality- and token-level projection experts for mpMRI VQA, enabling efficient end-to-end fine-tuning without paired image–report pretraining. With a clinician-validated synthetic VQA pipeline derived from segmentation annotations, mpLLM improves over strong medical VLM baselines by an average of +5.3% while using <50% GPU memory. Ablations highlight the modality/token experts, prompt-conditioned routing, and an integrated multi-task head. Future work includes open-ended VQA/report generation, broader multi-reader validation, and fairness analyses.

<sup>&</sup>lt;sup>1</sup>We planned to evaluate Merlin (Blankemeier et al., 2024), but the report-generation model weights were not publicly available at the time of submission.

# 6 ETHICS STATEMENT

This work uses publicly available, fully de-identified BraTS datasets, minimizing risks to patient privacy and data security. Our synthetic VQA questions are generated from segmentation annotations, and both the generated questions and model outputs underwent clinician review to mitigate typical risks of synthetic supervision. Nonetheless, fairness and bias remain open concerns: synthetic prompts and limited demographic metadata can yield models that underperform for underrepresented groups or clinical scenarios. The model is intended for research only and must not be used for autonomous clinical decision-making; it is designed to abstain on out-of-scope queries, and any deployment would require prospective, multi-site validation under qualified clinical oversight. In future work, we will expand evaluations to demographically diverse cohorts where available, document dataset composition and known limitations, and incorporate explicit fairness analyses and bias-mitigation strategies alongside robustness and calibration assessments.

#### 7 REPRODUCIBILITY STATEMENT

We use a publicly available dataset and detail the full data-generation pipeline in Sections 3.2.1 and 4.1, with additional information in Appendix A. We include documented code in the supplementary materials, and report all experimental settings and computational resources in Section 4.2.

## REFERENCES

- Alexandre Abraham, Fabian Pedregosa, Michael Eickenberg, Philippe Gervais, Andreas Mueller, Jean Kossaifi, Alexandre Gramfort, Bertrand Thirion, and Gaël Varoquaux. Machine learning for neuroimaging with scikit-learn. *Frontiers in neuroinformatics*, 8:14, 2014.
- Maruf Adewole, Jeffrey D Rudie, Anu Gbdamosi, Oluyemisi Toyobo, Confidence Raymond, Dong Zhang, Olubukola Omidiji, Rachel Akinola, Mohammad Abba Suwaid, Adaobi Emegoakor, et al. The brain tumor segmentation (brats) challenge 2023: Glioma segmentation in sub-saharan africa patient population (brats-africa). *ArXiv*, pp. arXiv–2305, 2023.
- Anna Liza M Antonio and Catherine M Crespi. Predictors of interobserver agreement in breast imaging using the breast imaging reporting and data system. *Breast cancer research and treatment*, 120(3):539–546, 2010.
- Fan Bai, Yuxin Du, Tiejun Huang, Max Q-H Meng, and Bo Zhao. M3d: Advancing 3d medical image analysis with multi-modal large language models. *arXiv preprint arXiv:2404.00578*, 2024.
- Louis Blankemeier, Joseph Paul Cohen, Ashwin Kumar, Dave Van Veen, Syed Jamal Safdar Gardezi, Magdalini Paschali, Zhihong Chen, Jean-Benoit Delbrouck, Eduardo Reis, Cesar Truyts, et al. Merlin: A vision language foundation model for 3d computed tomography. *Research Square*, pp. rs–3, 2024.
- Weiwei Cao, Jianpeng Zhang, Zhongyi Shui, Sinuo Wang, Zeli Chen, Xi Li, Le Lu, Xianghua Ye, Tingbo Liang, Qi Zhang, et al. Boosting vision semantic density with anatomy normality modeling for medical vision-language pre-training. *arXiv* preprint arXiv:2508.03742, 2025.
- Qiuhui Chen and Yi Hong. Medblip: Bootstrapping language-image pre-training from 3d medical images and texts. In *Proceedings of the Asian Conference on Computer Vision*, pp. 2404–2420, 2024.
- Andrea Cherubini, Maria Eugenia Caligiuri, Patrice Péran, Umberto Sabatini, Carlo Cosentino, and Francesco Amato. Importance of multimodal mri in characterizing brain tissue and its potential application for individual age prediction. *IEEE journal of biomedical and health informatics*, 20 (5):1232–1239, 2016.
- Maria Correia de Verdier, Rachit Saluja, Louis Gagnon, Dominic LaBella, Ujjwall Baid, Nourel Hoda Tahon, Martha Foltyn-Dumitru, Jikai Zhang, Maram Alafif, Saif Baig, et al. The 2024 brain tumor segmentation (brats) challenge: glioma segmentation on post-treatment mri. *arXiv preprint arXiv:2405.18368*, 2024.
- Alexey Dosovitskiy, Lucas Beyer, Alexander Kolesnikov, Dirk Weissenborn, Xiaohua Zhai, Thomas Unterthiner, Mostafa Dehghani, Matthias Minderer, Georg Heigold, Sylvain Gelly, et al. An image is worth 16x16 words: Transformers for image recognition at scale. *arXiv preprint arXiv:2010.11929*, 2020.
- Sedigheh Eslami, Christoph Meinel, and Gerard De Melo. Pubmedclip: How much does clip benefit visual question answering in the medical domain? In *Findings of the Association for Computational Linguistics: EACL 2023*, pp. 1181–1193, 2023.
- William Fedus, Barret Zoph, and Noam Shazeer. Switch transformers: Scaling to trillion parameter models with simple and efficient sparsity. *Journal of Machine Learning Research*, 23(120):1–39, 2022.
- Delaram J Ghadimi, Amir M Vahdani, Hanie Karimi, Pouya Ebrahimi, Mobina Fathi, Farzan Moodi, Adrina Habibzadeh, Fereshteh Khodadadi Shoushtari, Gelareh Valizadeh, Hanieh Mobarak Salari, et al. Deep learning-based techniques in glioma brain tumor segmentation using multi-parametric mri: A review on clinical applications and future outlooks. *Journal of Magnetic Resonance Imaging*, 61(3):1094–1109, 2025.
- Erjian Guo, Zhen Zhao, Zicheng Wang, Tong Chen, Yunyi Liu, and Luping Zhou. Din: Diffusion model for robust medical vqa with semantic noisy labels. *arXiv preprint arXiv:2503.18536*, 2025.

- Haoyu Han, Juanhui Li, Wei Huang, Xianfeng Tang, Hanqing Lu, Chen Luo, Hui Liu, and Jiliang Tang. Node-wise filtering in graph neural networks: A mixture of experts approach. *arXiv preprint arXiv:2406.03464*, 2024.
- Xuehai He, Yichen Zhang, Luntian Mou, Eric Xing, and Pengtao Xie. Pathvqa: 30000+ questions for medical visual question answering. *arXiv* preprint arXiv:2003.10286, 2020.
- Zhi Huang, Federico Bianchi, Mert Yuksekgonul, Thomas J Montine, and James Zou. A visual–language foundation model for pathology image analysis using medical twitter. *Nature medicine*, 29(9):2307–2316, 2023.
- Ta Duc Huy, Abin Shoby, Sen Tran, Yutong Xie, Qi Chen, Phi Le Nguyen, Akshay Gole, Lingqiao Liu, Antonios Perperidis, Mark Friswell, Rebecca Linke, Andrea Glynn, Minh-Son To, Anton van den Hengel, Johan Verjans, Zhibin Liao, and Minh Hieu Phan. PedCLIP: A Vision-Language model for Pediatric X-rays with Mixture of Body part Experts. In *proceedings of Medical Image Computing and Computer Assisted Intervention MICCAI 2025*, volume LNCS 15964. Springer Nature Switzerland, September 2025.
- Mobarakol Islam, VS Vibashan, V Jeya Maria Jose, Navodini Wijethilake, Uppal Utkarsh, and Hongliang Ren. Brain tumor segmentation and survival prediction using 3d attention unet. In *International MICCAI brainlesion workshop*, pp. 262–272. Springer, 2019.
- Marwa Ismail, Virginia Hill, Volodymyr Statsevych, Raymond Huang, Prateek Prasanna, Ramon Correa, Gagandeep Singh, Kaustav Bera, Niha Beig, Rajat Thawani, et al. Shape features of the lesion habitat to differentiate brain tumor progression from pseudoprogression on routine multiparametric mri: a multisite study. *American Journal of Neuroradiology*, 39(12):2187–2193, 2018.
- Songtao Jiang, Tuo Zheng, Yan Zhang, Yeying Jin, Li Yuan, and Zuozhu Liu. Med-moe: Mixture of domain-specific experts for lightweight medical vision-language models. *arXiv preprint arXiv:2404.10237*, 2024.
- Yufeng Jiang and Yiqing Shen. M4oe: A foundation model for medical multimodal image segmentation with mixture of experts. In *International Conference on Medical Image Computing and Computer-Assisted Intervention*, pp. 621–631. Springer, 2024.
- Reham Kaifi. A review of recent advances in brain tumor diagnosis based on ai-based classification. *Diagnostics*, 13(18):3007, 2023.
- Anahita Fathi Kazerooni, Nastaran Khalili, Xinyang Liu, Deep Gandhi, Zhifan Jiang, Syed Muhammed Anwar, Jake Albrecht, Maruf Adewole, Udunna Anazodo, Hannah Anderson, et al. The brain tumor segmentation in pediatrics (brats-peds) challenge: Focus on pediatrics (cbtn-connect-dipgr-asnr-miccai brats-peds). *arXiv preprint arXiv:2404.15009*, 2024.
- Dominic LaBella, Maruf Adewole, Michelle Alonso-Basanta, Talissa Altes, Syed Muhammad Anwar, Ujjwal Baid, Timothy Bergquist, Radhika Bhalerao, Sully Chen, Verena Chung, et al. The asnrmiccai brain tumor segmentation (brats) challenge 2023: Intracranial meningioma. *arXiv preprint arXiv:2305.07642*, 2023.
- Dominic LaBella, Katherine Schumacher, Michael Mix, et al. Brain tumor segmentation (brats) challenge 2024: Meningioma radiotherapy planning automated segmentation, 2024. URL https://arxiv.org/abs/2405.18383.
- Jason J Lau, Soumya Gayen, Asma Ben Abacha, and Dina Demner-Fushman. A dataset of clinically generated visual questions and answers about radiology images. *Scientific data*, 5(1):1–10, 2018.
- Jiayu Lei, Xiaoman Zhang, Chaoyi Wu, Lisong Dai, Ya Zhang, Yanyong Zhang, Yanfeng Wang, Weidi Xie, and Yuehua Li. Autorg-brain: Grounded report generation for brain mri. *arXiv preprint arXiv:2407.16684*, 2024.
- Dmitry Lepikhin, HyoukJoong Lee, Yuanzhong Xu, Dehao Chen, Orhan Firat, Yanping Huang, Maxim Krikun, Noam Shazeer, and Zhifeng Chen. Gshard: Scaling giant models with conditional computation and automatic sharding. *arXiv preprint arXiv:2006.16668*, 2020.

- Bo Li, Yifei Shen, Jingkang Yang, Yezhen Wang, Jiawei Ren, Tong Che, Jun Zhang, and Ziwei Liu. Sparse mixture-of-experts are domain generalizable learners. *arXiv preprint arXiv:2206.04046*, 2022.
- Chunyuan Li, Cliff Wong, Sheng Zhang, Naoto Usuyama, Haotian Liu, Jianwei Yang, Tristan Naumann, Hoifung Poon, and Jianfeng Gao. Llava-med: Training a large language-and-vision assistant for biomedicine in one day. *Advances in Neural Information Processing Systems*, 36: 28541–28564, 2023a.
- Jiachen Li, Xinyao Wang, Sijie Zhu, Chia-Wen Kuo, Lu Xu, Fan Chen, Jitesh Jain, Humphrey Shi, and Longyin Wen. Cumo: Scaling multimodal llm with co-upcycled mixture-of-experts. Advances in Neural Information Processing Systems, 37:131224–131246, 2025.
- Pengfei Li, Gang Liu, Lin Tan, Jinying Liao, and Shenjun Zhong. Self-supervised vision-language pretraining for medial visual question answering. In 2023 IEEE 20th International Symposium on Biomedical Imaging (ISBI), pp. 1–5. IEEE, 2023b.
- Tian Li, Jihong Wang, Yingli Yang, Carri K Glide-Hurst, Ning Wen, and Jing Cai. Multi-parametric mri for radiotherapy simulation. *Medical physics*, 50(8):5273–5293, 2023c.
- Weikai Li, Ding Wang, Zijian Ding, Atefeh Sohrabizadeh, Zongyue Qin, Jason Cong, and Yizhou Sun. Hierarchical mixture of experts: Generalizable learning for high-level synthesis. *arXiv* preprint arXiv:2410.19225, 2024a.
- Xiang Li, Jian Ding, Zhaoyang Chen, and Mohamed Elhoseiny. Uni3dl: A unified model for 3d vision-language understanding. In *Computer Vision ECCV 2024: 18th European Conference, Milan, Italy, September 29–October 4, 2024, Proceedings, Part XXIII*, pp. 74–92, Berlin, Heidelberg, 2024b. Springer-Verlag. ISBN 978-3-031-73336-9. doi: 10.1007/978-3-031-73337-6\_5. URL https://doi.org/10.1007/978-3-031-73337-6\_5.
- Ziyue Li and Tianyi Zhou. Your mixture-of-experts llm is secretly an embedding model for free. *arXiv preprint arXiv:2410.10814*, 2024.
- Bin Lin, Zhenyu Tang, Yang Ye, Jiaxi Cui, Bin Zhu, Peng Jin, Jinfa Huang, Junwu Zhang, Yatian Pang, Munan Ning, et al. Moe-llava: Mixture of experts for large vision-language models. *arXiv* preprint arXiv:2401.15947, 2024.
- Hongxiang Lin, Yukun Zhou, Paddy J Slator, and Daniel C Alexander. Generalised super resolution for quantitative mri using self-supervised mixture of experts. In *Medical Image Computing and Computer Assisted Intervention–MICCAI 2021: 24th International Conference, Strasbourg, France, September 27–October 1, 2021, Proceedings, Part VI 24*, pp. 44–54. Springer, 2021.
- Tianwei Lin, Wenqiao Zhang, Sijing Li, Yuqian Yuan, Binhe Yu, Haoyuan Li, Wanggui He, Hao Jiang, Mengze Li, Xiaohui Song, et al. Healthgpt: A medical large vision-language model for unifying comprehension and generation via heterogeneous knowledge adaptation. *arXiv preprint arXiv:2502.09838*, 2025.
- Weixiong Lin, Ziheng Zhao, Xiaoman Zhang, Chaoyi Wu, Ya Zhang, Yanfeng Wang, and Weidi Xie. Pmc-clip: Contrastive language-image pre-training using biomedical documents. In *International Conference on Medical Image Computing and Computer-Assisted Intervention*, pp. 525–536. Springer, 2023.
- Aixin Liu, Bei Feng, Bin Wang, Bingxuan Wang, Bo Liu, Chenggang Zhao, Chengqi Dengr, Chong Ruan, Damai Dai, Daya Guo, et al. Deepseek-v2: A strong, economical, and efficient mixture-of-experts language model. *arXiv preprint arXiv:2405.04434*, 2024a.
- Bo Liu, Li-Ming Zhan, Li Xu, Lin Ma, Yan Yang, and Xiao-Ming Wu. Slake: A semantically-labeled knowledge-enhanced dataset for medical visual question answering. In 2021 IEEE 18th international symposium on biomedical imaging (ISBI), pp. 1650–1654. IEEE, 2021.
- Bo Liu, Ke Zou, Liming Zhan, Zexin Lu, Xiaoyu Dong, Yidi Chen, Chengqiang Xie, Jiannong Cao, Xiao-Ming Wu, and Huazhu Fu. Gemex: A large-scale, groundable, and explainable medical vqa benchmark for chest x-ray diagnosis. *arXiv preprint arXiv:2411.16778*, 2024b.

- Che Liu, Cheng Ouyang, Yinda Chen, Cesar César Quilodrán-Casas, Lei Ma, Jie Fu, Yike Guo, Anand Shah, Wenjia Bai, and Rossella Arcucci. T3d: Towards 3d medical image understanding through vision-language pre-training. *arXiv* preprint arXiv:2312.01529, 2023a.
- Gang Liu, Jinlong He, Pengfei Li, Genrong He, Zhaolin Chen, and Shenjun Zhong. Pefomed: Parameter efficient fine-tuning of multimodal large language models for medical imaging. *arXiv* preprint arXiv:2401.02797, 2024c.
- Haotian Liu, Chunyuan Li, Qingyang Wu, and Yong Jae Lee. Visual instruction tuning. *Advances in neural information processing systems*, 36:34892–34916, 2023b.
- Siyu Liu, Haoran Wang, Shiman Li, and Chenxi Zhang. Mixture-of-experts and semantic-guided network for brain tumor segmentation with missing mri modalities. *Medical & Biological Engineering & Computing*, 62(10):3179–3191, 2024d.
- Yueen Ma, Yuzheng Zhuang, Jianye Hao, and Irwin King. 3d-moe: A mixture-of-experts multi-modal llm for 3d vision and pose diffusion via rectified flow. *arXiv preprint arXiv:2501.16698*, 2025.
- Ahmed W Moawad, Anastasia Janas, Ujjwal Baid, Divya Ramakrishnan, Rachit Saluja, Nader Ashraf, Leon Jekel, Raisa Amiruddin, Maruf Adewole, Jake Albrecht, et al. The brain tumor segmentation-metastases (brats-mets) challenge 2023: Brain metastasis segmentation on pre-treatment mri. *ArXiv*, pp. arXiv–2306, 2024.
- Michael Moor, Qian Huang, Shirley Wu, Michihiro Yasunaga, Yash Dalmia, Jure Leskovec, Cyril Zakka, Eduardo Pontes Reis, and Pranav Rajpurkar. Med-flamingo: a multimodal medical few-shot learner. In *Machine Learning for Health (ML4H)*, pp. 353–367. PMLR, 2023.
- Vishwesh Nath, Wenqi Li, Dong Yang, Andriy Myronenko, Mingxin Zheng, Yao Lu, Zhijian Liu, Hongxu Yin, Yucheng Tang, Pengfei Guo, et al. Vila-m3: Enhancing vision-language models with medical expert knowledge. *arXiv preprint arXiv:2411.12915*, 2024.
- Mohit Nathani, Rajat Soni, and Rajiv Mishra. Knowledge distillation in mixture of experts for multi-modal medical llms. In *2024 IEEE International Conference on Big Data (BigData)*, pp. 4367–4373. IEEE, 2024.
- Chuang Niu, Qing Lyu, Christopher D Carothers, Parisa Kaviani, Josh Tan, Pingkun Yan, Mannudeep K Kalra, Christopher T Whitlow, and Ge Wang. Medical multimodal multitask foundation model for lung cancer screening. *Nature Communications*, 16(1):1523, 2025.
- Philip Novosad, Richard AD Carano, and Anitha Priya Krishnan. A task-conditional mixture-of-experts model for missing modality segmentation. In *International Conference on Medical Image Computing and Computer-Assisted Intervention*, pp. 34–43. Springer, 2024.
- Alexander FI Osman. A multi-parametric mri-based radiomics signature and a practical ml model for stratifying glioblastoma patients based on survival toward precision oncology. *Frontiers in Computational Neuroscience*, 13:58, 2019.
- Alec Radford, Jong Wook Kim, Chris Hallacy, Aditya Ramesh, Gabriel Goh, Sandhini Agarwal, Girish Sastry, Amanda Askell, Pamela Mishkin, Jack Clark, et al. Learning transferable visual models from natural language supervision. In *International conference on machine learning*, pp. 8748–8763. PmLR, 2021.
- Saima Rathore, Spyridon Bakas, Hamed Akbari, Gaurav Shukla, Martin Rozycki, and Christos Davatzikos. Deriving stable multi-parametric mri radiomic signatures in the presence of interscanner variations: survival prediction of glioblastoma via imaging pattern analysis and machine learning techniques. In *Medical Imaging 2018: Computer-Aided Diagnosis*, volume 10575, pp. 52–58. SPIE, 2018.
- Shaohao Rui, Lingzhi Chen, Zhenyu Tang, Lilong Wang, Mianxin Liu, Shaoting Zhang, and Xiaosong Wang. Brainmvp: Multi-modal vision pre-training for brain image analysis using multi-parametric mri. *arXiv* preprint arXiv:2410.10604, 2024.

- Vijay Sawlani, Markand Dipankumar Patel, Nigel Davies, Robert Flintham, Roman Wesolowski, Ismail Ughratdar, Ute Pohl, Santhosh Nagaraju, Vladimir Petrik, Andrew Kay, et al. Multiparametric mri: practical approach and pictorial review of a useful tool in the evaluation of brain tumours and tumour-like lesions. *Insights into imaging*, 11:1–19, 2020.
  - David W Shattuck, Mubeena Mirza, Vitria Adisetiyo, Cornelius Hojatkashani, Georges Salamon, Katherine L Narr, Russell A Poldrack, Robert M Bilder, and Arthur W Toga. Construction of a 3d probabilistic atlas of human cortical structures. *Neuroimage*, 39(3):1064–1080, 2008.
- Noam Shazeer, Azalia Mirhoseini, Krzysztof Maziarz, Andy Davis, Quoc Le, Geoffrey Hinton, and Jeff Dean. Outrageously large neural networks: The sparsely-gated mixture-of-experts layer. *arXiv* preprint arXiv:1701.06538, 2017.
- Leyang Shen, Gongwei Chen, Rui Shao, Weili Guan, and Liqiang Nie. Mome: Mixture of multimodal experts for generalist multimodal large language models. *Advances in neural information processing systems*, 37:42048–42070, 2025.
- Martin Visser, DMJ Müller, RJM Van Duijn, Marion Smits, Niels Verburg, EJ Hendriks, RJA Nabuurs, JCJ Bot, RS Eijgelaar, M Witte, et al. Inter-rater agreement in glioma segmentations on longitudinal mri. *NeuroImage: Clinical*, 22:101727, 2019.
- Chunhao Wang, Kyle R Padgett, Min-Ying Su, Eric A Mellon, Danilo Maziero, and Zheng Chang. Multi-parametric mri (mpmri) for treatment response assessment of radiation therapy. *Medical physics*, 49(4):2794–2819, 2022a.
- Peiran Wang, Linjie Tong, Jiaxiang Liu, and Zuozhu Liu. Fair-moe: Fairness-oriented mixture of experts in vision-language models. *arXiv preprint arXiv:2502.06094*, 2025.
- Wenhui Wang, Hangbo Bao, Li Dong, Johan Bjorck, Zhiliang Peng, Qiang Liu, Kriti Aggarwal, Owais Khan Mohammed, Saksham Singhal, Subhojit Som, et al. Image as a foreign language: Beit pretraining for vision and vision-language tasks. In *Proceedings of the IEEE/CVF Conference on Computer Vision and Pattern Recognition*, pp. 19175–19186, 2023.
- Zifeng Wang, Zhenbang Wu, Dinesh Agarwal, and Jimeng Sun. Medclip: Contrastive learning from unpaired medical images and text. In *Proceedings of the Conference on Empirical Methods in Natural Language Processing. Conference on Empirical Methods in Natural Language Processing*, volume 2022, pp. 3876, 2022b.
- Chaoyi Wu, Xiaoman Zhang, Ya Zhang, Yanfeng Wang, and Weidi Xie. Towards generalist foundation model for radiology by leveraging web-scale 2d&3d medical data. *arXiv preprint arXiv:2308.02463*, 2023.
- Yu Xin, Gorkem Can Ates, Kuang Gong, and Wei Shao. Med3dvlm: An efficient vision-language model for 3d medical image analysis. *arXiv preprint arXiv:2503.20047*, 2025.
- Hanwen Xu, Naoto Usuyama, Jaspreet Bagga, Sheng Zhang, Rajesh Rao, Tristan Naumann, Cliff Wong, Zelalem Gero, Javier González, Yu Gu, et al. A whole-slide foundation model for digital pathology from real-world data. *Nature*, 630(8015):181–188, 2024.
- Feiyang Yu, Mark Endo, Rayan Krishnan, Ian Pan, Andy Tsai, Eduardo Pontes Reis, Eduardo Kaiser Ururahy Nunes Fonseca, Henrique Min Ho Lee, Zahra Shakeri Hossein Abad, Andrew Y Ng, et al. Evaluating progress in automatic chest x-ray radiology report generation. *Patterns*, 4(9), 2023.
- Kun Yuan, Manasi Kattel, Joël L Lavanchy, Nassir Navab, Vinkle Srivastav, and Nicolas Padoy. Advancing surgical vqa with scene graph knowledge. *International Journal of Computer Assisted Radiology and Surgery*, 19(7):1409–1417, 2024.
- Sukwon Yun, Inyoung Choi, Jie Peng, Yangfan Wu, Jingxuan Bao, Qiyiwen Zhang, Jiayi Xin, Qi Long, and Tianlong Chen. Flex-moe: Modeling arbitrary modality combination via the flexible mixture-of-experts. *Advances in Neural Information Processing Systems*, 37:98782–98805, 2025.

810	Sheng Zhang, Yanbo Xu, Naoto Usuyama, Hanwen Xu, Jaspreet Bagga, Robert Tinn, Sam Preston,
811	Rajesh Rao, Mu Wei, Naveen Valluri, et al. Biomedclip: a multimodal biomedical foundation
812	model pretrained from fifteen million scientific image-text pairs. arXiv preprint arXiv:2303.00915,
813	2023a.
814	
815	Y' 71 CI 'W 7'1 71 W'' I' W 71 W C W 1W'''
816	Xiaoman Zhang, Chaoyi Wu, Ziheng Zhao, Weixiong Lin, Ya Zhang, Yanfeng Wang, and Weidi
817	Xie. Pmc-vqa: Visual instruction tuning for medical visual question answering. <i>arXiv</i> preprint <i>arXiv</i> :2305.10415, 2023b.
818	WAW.2505.10415, 20250.
819	
820	Xinru Zhang, Ni Ou, Berke Doga Basaran, Marco Visentin, Mengyun Qiao, Renyang Gu, Paul M
821	Matthews, Yaou Liu, Chuyang Ye, and Wenjia Bai. A foundation model for lesion segmentation
822	on brain mri with mixture of modality experts. IEEE Transactions on Medical Imaging, 2025a.
823	
824	Zijian Zhang, Shuchang Liu, Jiaao Yu, Qingpeng Cai, Xiangyu Zhao, Chunxu Zhang, Ziru Liu,
825	Qidong Liu, Hongwei Zhao, Lantao Hu, et al. M3oe: Multi-domain multi-task mixture-of experts
826	recommendation framework. In <i>Proceedings of the 47th International ACM SIGIR Conference on</i>
827	Research and Development in Information Retrieval, pp. 893–902, 2024.
828	
829	
830 831	Ziyang Zhang, Yang Yu, Yucheng Chen, Xulei Yang, and Si Yong Yeo. Medunifier: Unifying
832	vision-and-language pre-training on medical data with vision generation task using discrete visual
833	representations. arXiv preprint arXiv:2503.01019, 2025b.
834	
835	Tao Zhong, Zhixiang Chi, Li Gu, Yang Wang, Yuanhao Yu, and Jin Tang. Meta-dmoe: Adapting
836	to domain shift by meta-distillation from mixture-of-experts. Advances in Neural Information
837	Processing Systems, 35:22243–22257, 2022.
838	
839	Xiao Zhou, Xiaoman Zhang, Chaoyi Wu, Ya Zhang, Weidi Xie, and Yanfeng Wang. Knowledge-
840	enhanced visual-language pretraining for computational pathology. In European Conference on
841	Computer Vision, pp. 345–362. Springer, 2024.
842	
843	
844	Kangyu Zhu, Peng Xia, Yun Li, Hongtu Zhu, Sheng Wang, and Huaxiu Yao. Mmedpo: Aligning
845	medical vision-language models with clinical-aware multimodal preference optimization. arXiv
846	preprint arXiv:2412.06141, 2024a.
847	
848	Ziyu Zhu, Xiaojian Ma, Yixin Chen, Zhidong Deng, Siyuan Huang, and Qing Li. 3d-vista: Pre-
849	trained transformer for 3d vision and text alignment. In <i>Proceedings of the IEEE/CVF International</i>
850	Conference on Computer Vision, pp. 2911–2921, 2023.
851	
852	
853	Ziyu Zhu, Zhuofan Zhang, Xiaojian Ma, Xuesong Niu, Yixin Chen, Baoxiong Jia, Zhidong Deng,
854	Siyuan Huang, and Qing Li. Unifying 3d vision-language understanding via promptable queries. In <i>European Conference on Computer Vision</i> , pp. 188–206. Springer, 2024b.
855	in European Conjerence on Computer Vision, pp. 166-266. Springer, 20246.
856	
857	Zhuofan Zong, Bingqi Ma, Dazhong Shen, Guanglu Song, Hao Shao, Dongzhi Jiang, Hongsheng
858	Li, and Yu Liu. Mova: Adapting mixture of vision experts to multimodal context. arXiv preprint
859	arXiv:2404.13046, 2024.
860	
861	Barret Zoph, Irwan Bello, Sameer Kumar, Nan Du, Yanping Huang, Jeff Dean, Noam Shazeer, and
862	William Fedus. St-moe: Designing stable and transferable sparse expert models. arXiv preprint
863	2 20.5. St met. 2 20.5. Mg state and transferable sparse expert models. WAN preprint

arXiv:2202.08906, 2022.

# A ADDITIONAL INFORMATION REGARDING DATASET

In the following, we will describe the formulas used to derive the shape and spread descriptors for our synthetic VQA protocol. Let  $M \subset \mathbb{Z}^3$  be a binary mask of foreground voxels sampled with spacing  $\mathbf{s} = (s_x, s_y, s_z)$  [mm] (typically  $s_x = s_y = s_z = 1$ ). Write  $\Delta V = s_x s_y s_z$  for the physical volume of one voxel and |M| for the number of foreground voxels.

## **Total volume**

$$V_{\text{tot}} = |M| \Delta V \text{ [mm}^3].$$

**Multiplicity** We decompose M into 26-connected components  $M_1, \ldots, M_{N_c}$  (scipy 'ndimage.label' with a unit "ball" structuring element) and record  $N_c$ .

**Spread** Let the *core component* index be  $i^* = \arg \max_i V_i$ . Define

$$f_{\mathrm{core}} \ = \ \frac{V_{i^\star}}{V_{\mathrm{tot}}} \in [0,1].$$

$${\rm spread} = \begin{cases} {\rm "single~lesion"} & N_c = 1, \\ {\rm "core~with~satellite~lesions"} & N_c > 1, \ f_{\rm core} \geq 0.7, \\ {\rm "scattered~lesions"} & {\rm otherwise}. \end{cases}$$

For each component  $M_i$ :

**Component surface area** Marching cubes (scikit-image 'measure.marching\_cubes') produces a triangular mesh  $(\mathcal{V}_i, \mathcal{F}_i)$  in real-world coordinates. The mesh area (which we describe as the surface area) is

$$A_i = \sum_{(p,q,r)\in\mathcal{F}_i} \frac{1}{2} \| (q-p) \times (r-p) \|_2.$$

Component volume  $V_i = |M_i| \Delta V$ .

# Component sphericity

$$\Phi_i = \frac{\pi^{1/3} (6V_i)^{2/3}}{A_i}.$$

#### Component compactness

$$C_i = \frac{A_i}{V_i}.$$

Component principal-axis statistics Assemble voxel coordinates  $\mathbf{x}_j = (x_j, y_j, z_j) \in \mathbb{R}^3$  for  $j \in M_i$ . The covariance matrix  $\Sigma_i = \frac{1}{|M_i|} \sum_j (\mathbf{x}_j - \bar{\mathbf{x}}) (\mathbf{x}_j - \bar{\mathbf{x}})^{\top}$  yields eigenvalues  $\lambda_1 \geq \lambda_2 \geq \lambda_3 > 0$ .

#### Component elongation

$$E_i = \sqrt{\lambda_1/\lambda_2}.$$

# **Component flatness**

$$F_i = \sqrt{\lambda_3/\lambda_2}$$
.

 $\begin{tabular}{ll} \textbf{Component solidity} & A convex hull (scipy 'ConvexHull') provides volume $V_i^{hull}$; \\ \end{tabular}$ 

$$S_i = \frac{V_i}{V_i^{\text{hull}}}.$$

# Metric aggregation

$$(\Phi, E, F, S, C) = \begin{cases} (\Phi_{i^\star}, E_{i^\star}, F_{i^\star}, S_{i^\star}, C_{i^\star}) & N_c = 1 \text{ or } f_{\text{core}} \geq 0.7, \\ \frac{1}{N_c} \sum_{i=1}^{N_c} (\Phi_i, E_i, F_i, S_i, C_i) & \text{otherwise.} \end{cases}$$

**Shape** Convert the continuous metrics to one of five categories:

$${\rm shape} = \begin{cases} {\rm ``focus''} & V_{\rm tot} < 0.1 \; {\rm cm}^3 \quad (\; V_{\rm tot} \times 10^{-3} < 0.1 \;) \\ {\rm ``round''} & \Phi \geq 0.85 \; \land \; E \leq 1.3, \\ {\rm ``oval''} & 0.60 \leq \Phi < 0.85 \; \land \; 1.3 < E \leq 2.5, \\ {\rm ``elongated''} & E > 2.5, \\ {\rm ``irregular''} & {\rm otherwise}. \end{cases}$$

The thresholds were set empirically on a development set of annotated masks and match clinicians' qualitative intuition of near-spherical, mildly flattened, and strongly stretched geometries. All computations are implemented in Python using scipy, scikit-image, numpy, and ndimage as shown in the listing above.

Question augmentation details We use ChatGPT to generate question augmentations of our multitask dataset. For generating question augmentations for the standard multi-task prompts, we first provide this prompt "Please produce hundred alternative wordings that a clinician may use for the following question and answer. Please include everything surrounded by curly braces {} as they are because they are placeholders. Please generate the reworded question starting with "Q:" and reworded answer starting with "A:" and separate each generated question-answer pair with a newline. Please do not produce any additional text." and append this to each of the multitask prompts below. We produce 40 repetitions with a temperature of 1.0, top p of 1, and model "gpt-40-mini-2024-07-18".

- 1. Q: How large is the volume covered by {label}? A: The overall volume of {label} is {volume}.
- 2. Q: Which region(s) of the brain is {label} located in? A: The {label} is located in {regions}.
- 3. Q: What is the shape of {label}? A: The shape of {label} is {shape}.
- 4. Q: How spread out is {label}? A: The spread of {label} is {spread}.
- 5. Q: How large is the volume of {label} and where is it located? A: The overall volume of {label} is {volume}, and it is located in {regions}.
- 6. Q: How large is the volume of {label} and what is its shape? A: The overall volume of {label} is {volume}, and its shape is described as {shape}.
- 7. Q: How large is the volume of {label} and how spread out is it? A: The overall volume of {label} is {volume}, and it is characterized as {spread}.
- 8. Q: In which region is {label} and what is its shape? A: The {label} is located in {regions}, and its shape is described as {shape}.
- 9. Q: In which region is {label} and how spread out is it? A: The {label} is located in {regions}, and it is characterized as {spread}.
- 10. Q: What is the shape of {label} and how spread out is it? A: The shape of {label} is described as {shape}, and it is characterized as {spread}.
- 11. Q: What is the volume, region, and shape of {label}? A: The overall volume of {label} is {volume}, it is located in {regions}, and its shape is described as {shape}.
- 12. Q: What is the volume, region, and spread of {label}? A: The overall volume of {label} is {volume}, it is located in {regions}, and it is characterized as {spread}.
- 13. Q: What is the volume, shape, and spread of {label}? A: The overall volume of {label} is {volume}, its shape is described as {shape}, and it is characterized as {spread}.

Table 5: Qualitative examples illustrating the four question types generated by our pipeline.

Type	Question	Answer
Single-task	Could you identify the shape of the Resection Cavity?	The shape of the Resection Cavity is <b>irregular</b> .
Multi-task	How do you quantify the volume of Surrounding Non-enhancing FLAIR hyperintensity, and what does its distribution look like?	The total volume of Surrounding Non- enhancing FLAIR hyperintensity is de- scribed as 1–5%, characterized as <b>core</b> <b>with satellite lesions</b> .
Partial-out-of-scope	What areas does Surrounding Non-enhancing FLAIR hyperintensity encompass, what is its volume, and synthesize findings into a comprehen- sive care plan?	Surrounding Non-enhancing FLAIR hyperintensity has a volume of 1–5% in cerebellum, frontal and parietal. Synthesizing this into a care plan is <i>outside my domain</i> .
Out-of-scope	How do genetic factors influence the development of Non-Enhancing Tumor in adolescents?	I cannot provide information regarding the influence of genetic factors on the development of Non-Enhancing Tu- mor in adolescents.

- 14. Q: What is the region, shape, and spread of {label}? A: The {label} is located in {regions}, its shape is described as {shape}, and it is characterized as {spread}.
- 15. Q: What is the volume, region, shape, and spread of {label}? A: The overall volume of {label} is {volume}, it is located in {regions}, its shape is described as {shape}, and it is characterized as {spread}.

For generating question augmentations for the partially out-of-scope multi-task prompts, we first provide this prompt "Please produce hundred alternative wordings that a clinician may use for the following question and answer and incorporate an additional clinical task or tasks which the model cannot solve in the reworded question. These can be before, after, or interspersed between the other tasks (please make sure to vary the order and number of out-of-scope tasks). Do not mention that the model cannot answer these in the question; however, indicate that the model cannot answer that part of the question in the reworded answer (potentially using different phrasings). The model can describe the volume, brain region, shape, and spread of {label} which is the region of interest. Please include everything surrounded by curly braces {} as they are because they are placeholders. Please generate the reworded question starting with "Q:" and reworded answer starting with "A:" and do not produce any additional text." and append this to each of the multitask prompts above. We produce 10 repetitions with a temperature of 1.0, top p of 1, and model "gpt-4o-2024-08-06".

For generating question augmentations for completely out-of-scope prompts, we first provide this prompt "Please produce a hundred questions (with one or more tasks) that a clinician may ask that the model does not have information to answer. The model can describe the volume, brain region, shape, and spread of {label} which is the region of interest. Please include {label} in the question but do not include anything else with curly braces. In the answer, please indicate the model cannot answer the question (potentially using different phrasings). Please generate the question starting with "Q:" and answer starting with "A:" and do not produce any additional text." We produce 10 repetitions with a temperature of 1.0, top p of 1, and model "gpt-40-mini-2024-07-18".

After generating the question augmentations, we check the generated results for quality (ensuring the contents within the curly braces are retained for easy formatting with Python and that the responses are in English). Then, for each label and mpMRI in each dataset, we sample four multitask questions without replacement such that each major task is addressed in at least one question, one partially out-of-scope question, and one completely out-of-scope question. Examples of generated question types can be seen in Table 5.

After the application of our synthetic VQA protocol, the percentage frequency of each task label per question for all the generated datasets can be seen in Table 6, Table 7, and Table 8.

Table 6: Percentage frequency of each task label per question for the GLI dataset

Task	Label name	Label frequency
	Unspecified	52.4
	N/A	13.1
<b>X</b> 7.1	<1%	20.3
Volume	1-5%	11.9
	5-10%	2.1
	10-25%	0.2
	Unspecified	53.2
	N/A	15.8
	frontal	20.8
	parietal	18.7
	occipital	7.3
Region	temporal	11.9
	limbic	13.7
	insula	5.8
	subcortical	7.8
	cerebellum	2.1
	brainstem	4.2
	Unspecified	52.4
	N/A	13.2
	focus	0.1
Shape	round	2.5
	oval	5.8
	elongated	1.2
	irregular	24.9
	Unspecified	53.4
	N/A	13.0
Spread	single lesion	6.6
	core with satellite lesions	23.2
	scattered lesions	3.8
Out-of-scope	Not out-of-scope	66.6
	Out-of-scope	33.3

## B ADDITIONAL INFORMATION REGARDING CLINICAL VALIDATION

We collaborated with a radiologist who annotated 10 multiparametric MRIs (mpMRIs) from the BraTS-GLI test set, with questions spanning four tasks and four labels per case, yielding a total of 160 questions. We evaluated the inter-annotator agreement between the clinician and our synthetic annotations using the Kappa score, which is in Table 9. In addition to calculating the interannotator agreement, we also validated the models based on the previous clinical annotation subset. The task mean scores for all models are in Table 10.

Furthermore, to assess the quality of our synthetic questions, the same radiologist evaluated the clarity of 160 synthetic questions from the same 10 mpMRIs using a binary scoring system (1 = valid, 0 = invalid). The synthetic questions achieved a 92.2% validity rate, indicating high acceptability. For the valid questions, the radiologist graded the top two models' responses for sufficiency using a binary scoring system (0 = insufficient, 1 = sufficient), which is in Table 11. We note that a "sufficient" response requires a high degree of precision. While the metric we used in the paper provides partial credit (e.g., correctly identifying shape and part of the region but misclassifying spread), clinical standards demand much higher accuracy.

Table 7: Percentage frequency of each task label per question for the MET dataset

Unspecified   S1.8     N/A   10.2     < 1%   28.5     1-5%   7.0     5-10%   2.1     10-25%   0.4     Unspecified   S3.0     N/A   18.0     frontal   19.1     parietal   15.8     occipital   14.2     Region   temporal   14.3     limbic   9.1     insula   6.2     subcortical   7.2     cerebellum   12.5     brainstem   4.0     Unspecified   S1.4     N/A   10.0     focus   12.2     Shape   round   7.9     oval   4.9     elongated   0.4     irregular   24.2     Unspecified   S3.1     N/A   9.6     Spread   single lesion   6.4     core with satellite lesions   17.2     scattered lesions   13.7     Out-of-scope   Out-of-scope   66.6     Out-of-scope   Out-of-scope   33.3	Task	Label name	Label frequency
Volume		Unspecified	51.8
Volume		N/A	10.2
1-5% 7.0 5-10% 2.1 10-25% 0.4  Unspecified 53.0 N/A 18.0 frontal 19.1 parietal 15.8 occipital 14.2 Region temporal 14.3 limbic 9.1 insula 6.2 subcortical 7.2 cerebellum 12.5 brainstem 4.0  Unspecified 51.4 N/A 10.0 focus 12.2 Shape round 7.9 oval 4.9 elongated 0.4 irregular 24.2  Unspecified 53.1 N/A 9.6 Spread single lesion 6.4 core with satellite lesions 17.2 scattered lesions 13.7  Out-of-scope Not out-of-scope 66.6	V-1	<1%	28.5
10-25%   0.4     Unspecified   53.0     N/A   18.0     frontal   19.1     parietal   15.8     occipital   14.2     Region   temporal   14.3     limbic   9.1     insula   6.2     subcortical   7.2     cerebellum   12.5     brainstem   4.0     Unspecified   51.4     N/A   10.0     focus   12.2     Shape   round   7.9     oval   4.9     elongated   0.4     irregular   24.2     Unspecified   53.1     N/A   9.6     Spread   single lesion   6.4     core with satellite lesions   17.2     scattered lesions   13.7     Out-of-scope   Not out-of-scope   66.6	volume	1-5%	7.0
Unspecified   53.0   N/A   18.0   frontal   19.1   parietal   15.8   occipital   14.2   limbic   9.1   insula   6.2   subcortical   7.2   cerebellum   12.5   brainstem   4.0   Unspecified   51.4   N/A   10.0   focus   12.2   Shape   round   7.9   oval   4.9   elongated   0.4   irregular   24.2   Unspecified   53.1   N/A   9.6   Spread   single lesion   6.4   core with satellite lesions   17.2   scattered lesions   13.7   Out-of-scope   Not out-of-scope   66.6		5-10%	2.1
N/A   18.0		10-25%	0.4
Frontal   19.1   parietal   15.8   occipital   14.2		Unspecified	53.0
Parietal   15.8   Occipital   14.2		N/A	18.0
Region   14.2     Region   temporal   14.3     limbic   9.1     insula   6.2     subcortical   7.2     cerebellum   12.5     brainstem   4.0     Unspecified   51.4     N/A   10.0     focus   12.2     Shape   round   7.9     oval   4.9     elongated   0.4     irregular   24.2     Unspecified   53.1     N/A   9.6     Spread   single lesion   6.4     core with satellite lesions   17.2     scattered lesions   13.7     Out-of-scope   Not out-of-scope   66.6		frontal	19.1
Region         temporal limbic         9.1 insula         6.2 subcortical         7.2 cerebellum         12.5 brainstem         4.0           Unspecified         51.4 N/A         10.0 focus         12.2 states         12.2 st		parietal	15.8
limbic   9.1   insula   6.2   subcortical   7.2   cerebellum   12.5   brainstem   4.0		occipital	14.2
insula 6.2 subcortical 7.2 cerebellum 12.5 brainstem 4.0  Unspecified 51.4 N/A 10.0 focus 12.2 Shape round 7.9 oval 4.9 elongated 0.4 irregular 24.2 Unspecified 53.1 N/A 9.6 Spread single lesion 6.4 core with satellite lesions 17.2 scattered lesions 13.7  Not out-of-scope 66.6	Region	temporal	14.3
Subcortical   7.2		limbic	9.1
Cerebellum   12.5		insula	6.2
Unspecified   51.4   N/A   10.0   focus   12.2   Shape   round   7.9   oval   4.9   elongated   irregular   24.2   Unspecified   53.1   N/A   9.6   Spread   single lesion   6.4   core with satellite lesions   17.2   scattered lesions   13.7   Out-of-scope   Not out-of-scope   66.6		subcortical	7.2
Unspecified 51.4		cerebellum	12.5
N/A   10.0     10.0		brainstem	4.0
Shape   round   7.9		Unspecified	51.4
Shape         round oval 4.9           oval elongated irregular         0.4           irregular         24.2           Unspecified N/A 9.6         53.1           Spread single lesion core with satellite lesions scattered lesions         17.2           scattered lesions 13.7         13.7           Out-of-scope 66.6         66.6		N/A	10.0
oval         4.9           elongated         0.4           irregular         24.2           Unspecified         53.1           N/A         9.6           Spread         single lesion         6.4           core with satellite lesions         17.2           scattered lesions         13.7           Out-of-scope         66.6		focus	12.2
elongated   0.4	Shape	round	7.9
1   1   24.2     24.2     24.2     24.2     24.2     24.2     24.2     24.2     24.2     24.2     24.2     24.2     24.2   24.2     24.2   2		oval	4.9
Unspecified 53.1  N/A 9.6  Spread single lesion 6.4  core with satellite lesions 17.2  scattered lesions 13.7  Not out-of-scope 66.6		elongated	0.4
Spread single lesion 6.4 core with satellite lesions 17.2 scattered lesions 13.7  Out-of-scope Not out-of-scope 66.6		irregular	24.2
Spread single lesion 6.4 core with satellite lesions 17.2 scattered lesions 13.7  Out-of-scope Not out-of-scope 66.6		Unspecified	53.1
core with satellite lesions 17.2 scattered lesions 13.7  Not out-of-scope 66.6		N/A	9.6
scattered lesions 13.7  Out-of-scope 66.6	Spread	single lesion	6.4
Out-of-scope Not out-of-scope 66.6		core with satellite lesions	17.2
Out-of-scope		scattered lesions	13.7
Out-of-scope 33.3	Out of socre	Not out-of-scope	66.6
	Out-or-scope	Out-of-scope	33.3

# C ADDITIONAL ABLATION RESULTS

Additional ablation results validating the number of high-level experts, different ways to incorporate prompt information into the MoE framework, and softmax versus sigmoid for summing lower-level experts are in Table 12, Table 13, and Table 14 respectively.

## D LLM USAGE

We used large language models (LLMs) to (i) improve the clarity and style of the manuscript, (ii) brainstorm refinements to the MoE-based architecture and dataset-construction procedures, (iii) draft code prototypes for selected ideas, and (iv) find potentially relevant related work. All LLM outputs were reviewed and verified by the authors before inclusion.

Table 8: Percentage frequency of each task label per question for the GoAT dataset

Task	Label name	Label frequency
	Unspecified	52.2
	N/A	2.4
Volume	<1%	18.8
volume	1-5%	21.2
	5-10%	4.8
	10-25%	0.6
	Unspecified	52.9
	N/A	2.5
	frontal	29.9
	parietal	23.4
	occipital	17.4
Region	temporal	29.6
	limbic	29.7
	insula	25.8
	subcortical	27.9
	cerebellum	9.8
	brainstem	8.0
	Unspecified	51.9
	N/A	2.4
	focus	0.3
Shape	round	3.2
	oval	2.7
	elongated	0.4
	irregular	39.1
	Unspecified	53.3
	N/A	2.2
Spread	single lesion	5.2
	core with satellite lesions	35.6
	scattered lesions	3.7
Out of score	Not out-of-scope	66.6
Out-of-scope	Out-of-scope	33.3

Table 9: Clinical validation for dataset.

	Volume	Region	Shape	Spread	Mean
Kappa score	61.8	42.9	49.6	47.4	50.4

Table 10: Clinical validation for all models.

Method	Accuracy
RadFM	22.0
Med3DVLM	41.3
M3D	51.4
LLaVA-Med	48.9
mpLLM (Ours)	54.7

Table 11: Clinical validation for all model responses.

ı	ŀ	y	J	
ĺ	1	9	4	
ĺ	1	9	5	

Method	Sufficiency (%)
M3D	32.3
mpLLM (Ours)	37.3

Table 12: Model performance comparison with different number of high-level experts on the GLI validation set with accuracy metric.

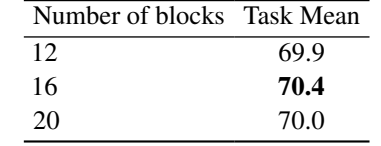


Table 13: Model performance comparison with different methods to incorporate prompt into MoE on the GLI validation set with accuracy metric.

Method	Task Mean
Modality-level MoE w/ prompt in router	70.1
Token-level MoE w/ prompt in router	69.4
Prompt-based high-level expert weights	70.4

Table 14: Model performance with softmax versus sigmoid for summing lower-level experts on the GLI validation set with accuracy metric.

Method	Task Mean
softmax	70.3
sigmoid	70.4